Small-Angle Scattering from Hexagonally Packed Cylindrical Particles with Paracrystalline Distortion

Takeji Hashimoto,* Tetsuya Kawamura,† Masafumi Harada,‡ and Hideaki Tanaka§

Division of Polymer Chemistry, Graduate School of Engineering, Kyoto University, Kyoto 606, Japan

Received October 25, 1993; Revised Manuscript Received March 3, 1994®

ABSTRACT: Elastic small-angle scattering of X-rays, neutrons, and light from an assembly of hexagonally packed cylindrical particles with a paracrystalline distortion was investigated. The scattering formula is presented, and the effects of the paracrystalline distortion factor g and volume fraction of the particles on the scattering profiles are discussed. This scattering theory is applied to small-angle X-ray scattering (SAXS) from a binary mixture of a sphere-forming block copolymer and a lamellar-forming block copolymer. The SAXS study confirmed that the two copolymers are mixed at the molecular level, forming the hexagonally packed cylindrical morphology, and the various characteristic parameters describing the morphology were extracted from the best fit between the experimental and theoretical scattering profiles. The SAXS results were confirmed by transmission electron microscopy.

I. Introduction

Elastic small-angle scattering (SAS) of X-rays, neutrons, and light has been used as one of the most powerful techniques in structural analyses of heterogeneous materials.[1] The technique has been applied to various fields in complex fluids (colloids, surfactants, emulsions, polymers, liquid crystals, membranes, etc.) as well as those in the solid state, and heterogeneities occurring in the length scale ranging from 10 Å to 10 μm have usually been studied.

We have previously presented SAS analyses of a one-dimensional stack of lamellae[2] and spherical particles stacked with cubic symmetries,[3] both with paracrystalline distortion.[4] We have discussed the effects of various structure parameters on SAS profiles[2,3,5] and applications of the SAS analyses to block copolymer systems with lamellar[2,6] and spherical microdomains[3,7] as well as to latex particles.[3] Here we extend our analyses to hexagonally packed cylindrical particles with paracrystalline distortion, and we apply our analyses to a block copolymer having the cylindrical microdomain.

In this paper we first present the scattering theory for an assembly of hexagonally packed cylindrical particles with a given orientation (sections II and III) and an arbitrary orientation distribution (section IV). We then discuss numerical analyses of the scattering profiles (section V). This scattering theory is applied to small-angle X-ray scattering (SAXS) from the block copolymer system polystyrene-*block*-poly(ethylenepropylene) (PS–PEP), particularly a binary mixture of the lamellar-forming PS–PEP and the sphere-forming PS–PEP (section VI). Comparisons between theoretical and experimental SAXS profiles prove that the two copolymers are mixed at the molecular level, forming hexagonally packed cylindrical microdomains. Comparisons also provide the various characteristic parameters describing the cylindrical systems.

* To whom correspondence should be addressed.

† Present address: Tonen Chemical Corp., Tonen Corporate R&D Laboratory, 1-3-1, Nishi-Tsurugaoka Ohi-machi, Iruma-gun, Saitama 356, Japan.

‡ Present address: Department of Industrial Chemistry, Faculty of Engineering, University of Tokyo, Hongo, Bunkyo-ku, Tokyo 113, Japan.

§ Present address: Mitsubishi Kasei Corp., Research Center, 1000 Kamoshida-cho, Midori-ku, Yokohama 227, Japan.

® Abstract published in *Advance ACS Abstracts,* April 15, 1994.

II. Scattering Theory

II-1. Model. Let $Oxyz$ be the Cartesian coordinate fixed to a grain of cylindrical particles with radius R and length L packed with hexagonal symmetry and with cell edge a (Figure 1a). We assume that the cylinders are perfectly oriented along the Oz axis in this grain as shown in Figure 1a,b, where $\mathbf{a}_1$ and $\mathbf{a}_2$ are the primitive lattice vectors whose magnitudes correspond to the intercylinder distance a. According to the conventional method, we transform the primitive lattice vectors $\mathbf{a}_1$, $\mathbf{a}_2$, and $\mathbf{a}_3$, where $\mathbf{a}_3$ is parallel to the Oz axis, into the orthogonal lattice vectors $\mathbf{b}_1$, $\mathbf{b}_2$, and $\mathbf{b}_3$, where $\mathbf{b}_1$, $\mathbf{b}_2$, and $\mathbf{b}_3$ are defined in Figure 1b,

$$\mathbf{b}_3 = \mathbf{a}_3 \tag{1a}$$

$$\mathbf{b}_2 = \mathbf{a}_2 \tag{1b}$$

$$\mathbf{b}_1 = 2\mathbf{a}_1 + \mathbf{a}_2 \tag{1c}$$

and take the Ox and Oy axes parallel to $\mathbf{b}_1$ and $\mathbf{b}_2$. For a perfect lattice we have

$$|\mathbf{a}_1| = |\mathbf{a}_2| = a \tag{2}$$

We assume that $\mathbf{a}_1$ and $\mathbf{a}_2$ have the paracrystalline distortion $(\Delta^2 a_{ij})^{1/2}$ $(i,j = 1,2)$ as shown in Figure 1c. In this work we shall give a numerical analysis only for a special case of the directionally independent paracrystalline distortions such that

$$\Delta^2 a_{ij} = \Delta^2 a \tag{3}$$

The grain contains N_1 and N_2 unit cells along $\mathbf{a}_1$ and $\mathbf{a}_2$, respectively, and only one unit cell along $\mathbf{a}_3$; hence there are $N = N_1 N_2$ cells in total. Thus our model does not apply to the case of smectic ordering, because it assumes no axial orientation correlation between the cylinders. The intergrain interference effect was ignored in our model, so that the scattered intensity (but not the scattered amplitude) from each grain is summed up ("*independent scattering*" assumption). This assumption of independent scattering is legitimate for scattering at $q > q^*$, where q is the magnitude of the scattering vector defined in section II-2-A. The quantity q^* is a critical value of q given by $q^* \equiv \max[2\pi/L, 2\pi/N_1 a, 2\pi/N_2 a]$. The grains have an orientation distribution which is specified by $w(\alpha,\Omega,\kappa)$ with respect to the Cartesian coordinate $Ox_1y_1z_1$ fixed to the

0024-9297/94/2227-3063$04.50/0

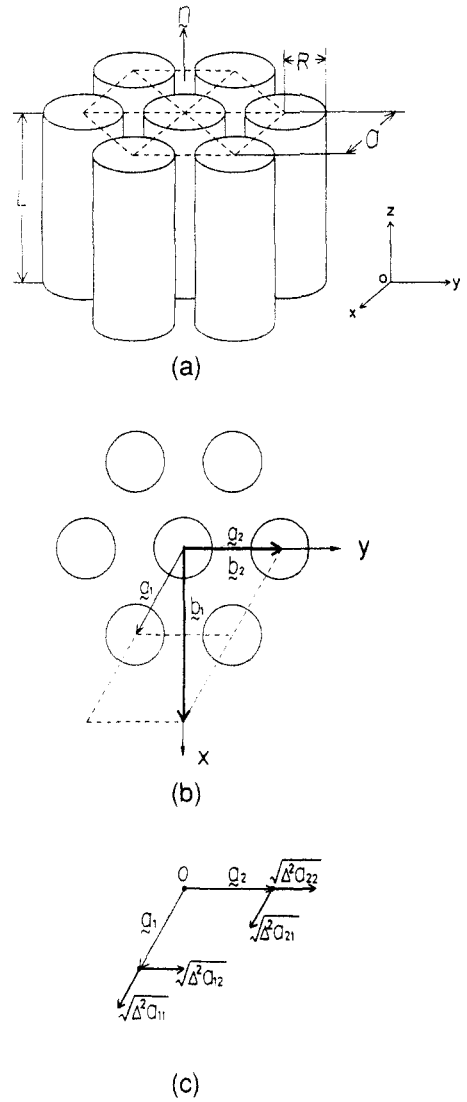

Figure 1. (a) An assembly of hexagonally packed cylinders of length L and radius R and the coordinate $Oxyz$ fixed to the assembly. (b) Relation between the primitive vectors ($\mathbf{a}_1$ and $\mathbf{a}_2$) and the orthogonal vectors ($\mathbf{b}_1$ and $\mathbf{b}_2$) for the hexagonal lattice. (c) Paracrystal distortions of the second kind $[\Delta^2 a_{ij}]^{1/2}$ $(i,j = 1,2)$. The axis Oz is parallel to the cylinder axis whose unit vector is given by $\mathbf{n}$. There is no axial orientation correlation of the cylinders along Oz.

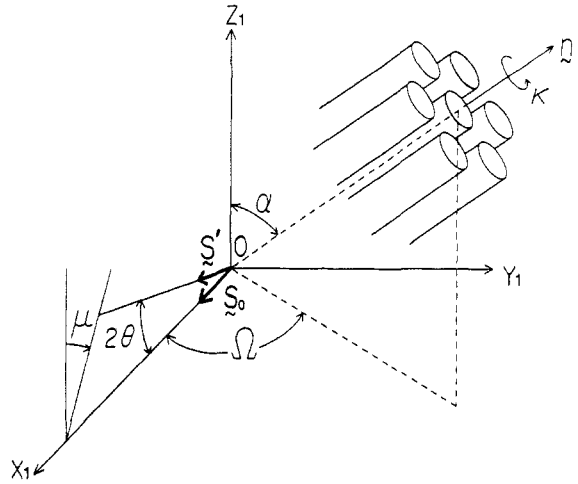

Figure 2. Eulerian angles (α,Ω,κ) which specify the orientation of the cylinder axis $\mathbf{n}$ with respect to a laboratory-fixed Cartesian coordinate $Ox_1y_1z_1$. Ox_1 is the incident beam axis, parallel to the unit vector $\mathbf{s}_0$, and the 2D detector is placed in the plane normal to $\mathbf{s}_0$. $\mathbf{s}'$ is the unit vector parallel to the scattered beam whose intensity is measured as a function of the scattering angle 2θ and azimuthal angle μ.

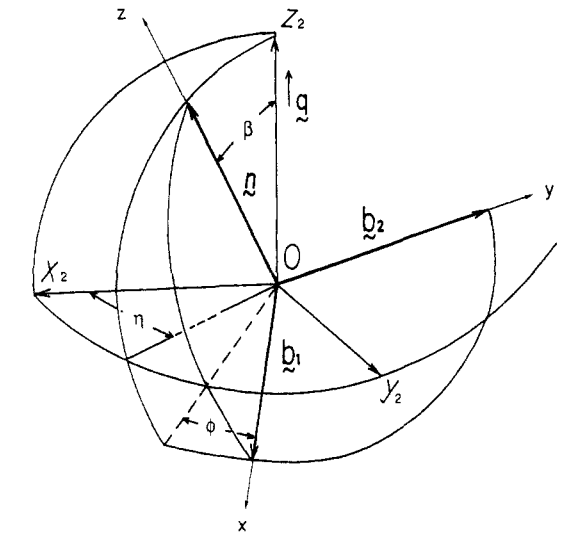

Figure 3. Eulerian angles (β,η,ϕ) which specify a relationship between the two Cartesian coordinates, $Oxyz$ fixed to the paracrystal and $Ox_2y_2z_2$ fixed to the laboratory. The axis Oz_2 is taken parallel to $\mathbf{q}$.

laboratory, as shown in Figure 2, or by $w(\beta,\eta,\phi)$ with respect to the Cartesian coordinate $Ox_2y_2z_2$ fixed to another laboratory coordinate. The properties of the grains are assumed to be independent of orientation. In Figures 2 and 3, $\mathbf{n}$ is a unit vector along the Oz axis, i.e., the cylindrical axis in the grain which has orientation specified by a polar angle α, an azimuthal angle Ω, and a rotational angle κ with respect to its axis $\mathbf{n}$. The incident beam propagates along the Ox_1 axis and its propagation direction is denoted by a unit vector $\mathbf{s}_0$. The intensity of the scattered beam, the propagation direction of which is specified by a unit vector $\mathbf{s}'$, is measured as a function of scattering angle 2θ and azimuthal angle μ.

II-2. Scattering Formula for Cylindrical Systems with Paracrystalline Distortion of the Second Kind. II-2-A. General Formula. Let $I(\mathbf{q};n)$ be the elastic scattering intensity at scattering vector $\mathbf{q}$ from the grain with a given orientation $\mathbf{n}$ with respect to the laboratory-fixed coordinate (Figure 2), where $\mathbf{q}$ is given by

$$\mathbf{q} = 2\pi(\mathbf{s}' - \mathbf{s}_0)/\lambda$$

with λ being the wavelength of the incident beam. Then $I(\mathbf{q};n)$ is generally given by[4]

$$I(\mathbf{q};\mathbf{n}) = N[\langle|f(\mathbf{q})|^2\rangle - |\langle f(\mathbf{q})\rangle|^2] + N|\langle f(\mathbf{q})\rangle|^2[1 - D^2(\mathbf{q})] + (1/v)|\langle f(\mathbf{q})\rangle|^2 D^2(\mathbf{q})\, Z(\mathbf{q})^* |\Sigma(\mathbf{q})|^2 \quad (4)$$

where N is the number of particles in the grain, $f(q)$ is the structure amplitude of the particle, v is the volume occupied per particle, $Z(\mathbf{q})$ is the paracrystal lattice factor with distortion of the second kind,[4] $\Sigma(\mathbf{q})$ is the shape amplitude of the grain, and $D^2(\mathbf{q})$ is the factor related to the thermal vibration about the paracrystalline lattice points, associated with the paracrystalline distortion of the first kind.[4] The symbol "*" designates a convolution product. $\langle|f(\mathbf{q})|^2\rangle$ and $\langle f(\mathbf{q})\rangle$ denote, respectively, an average of $|f(\mathbf{q})|^2$ and $f(\mathbf{q})$ with respect to size distribution, orientation distribution, and scattering power distribution of the cylinders in the lattice. Now $Z(\mathbf{q})$ is given by

$$Z(\mathbf{q}) = \prod_{k=1}^{d} Z_k(q) \quad (5)$$

where d is the spatial dimensionality ($d = 1$, 2, or 3); $d = 2$ for our system. The kth lattice factor $Z_k(\mathbf{q})$ is given by

$$Z_k(\mathbf{q}) = \mathrm{Re}\left\{\frac{1+F_k(\mathbf{q})}{1-F_k(\mathbf{q})}\right\} \tag{6a}$$

$$= \frac{1-|F_k|^2}{1-2|F_k|\cos(\mathbf{a}_k\cdot\mathbf{q})+|F_k|^2} \tag{6b}$$

with Re{x} designating the real part of x and

$$F_k(\mathbf{q}) = |F_k(\mathbf{q})|\exp(-i\mathbf{q}\cdot\mathbf{a}_k) \tag{7}$$

and

$$|F_k(\mathbf{q})| = \prod_{j=1}^{2}\exp\left[-\frac{1}{2}g_{kj}^2(\mathbf{q}\cdot\mathbf{a}_j)^2\right] \tag{8}$$

Here $\{g_{kj}\}$ $(k,j = 1,2)$ are components of the paracrystalline distortion tensor defined by

$$g_{kj}^2 = \Delta^2 a_{kj}/a_j^2 \tag{9}$$

where $\Delta^2 a_{kj}$ are defined in Figure 1c.

An alternative expression for eq 5 convenient for numerical calculations is given by

$$I(\mathbf{q};\mathbf{n}) = N[\langle|f|^2\rangle - |\langle f\rangle|^2] + N|\langle f\rangle|^2[1-D^2(\mathbf{q})] + |\langle f\rangle|^2 D^2(\mathbf{q})\prod_{k=1}^{d}N_k\left[Z_k + \frac{I_{ck}}{N_k}\right] \tag{10}$$

where I_{ck} is the zeroth-order scattering related to the finite size of the grain and is given by[8]

$$I_{ck} = -2\,\mathrm{Re}\frac{F_k(1-F_k^{N_k})}{(1-F_k)^2} \tag{11a}$$

$$= \frac{-2|F_k|}{\{1-2|F_k|\cos(\mathbf{q}\cdot\mathbf{a}_k)+|F_k|^2\}^2}\{(1+|F_k|^2)\cos(\mathbf{q}\cdot\mathbf{a}_k) - 2|F_k| - |F_k|^{N_k}\cos[(N_k+1)(\mathbf{q}\cdot\mathbf{a}_k)] + 2|F_k|^{N_k+1}\times \cos[N_k(\mathbf{q}\cdot\mathbf{a}_k)] - |F_k|^{N_k+2}\cos[(N_k-1)(\mathbf{q}\cdot\mathbf{a}_k)]\} \tag{11b}$$

Then the observed scattering intensity at $\mathbf{q}$, $I(\mathbf{q})$, is given by

$$I(q) = \langle I(\mathbf{q};\mathbf{n})\rangle_n \tag{12}$$

where $\langle\ldots\rangle_n$ designates the scattered intensity averaged over all possible orientation distributions of $\mathbf{n}$, specified by the distribution function $w(\alpha,\Omega,\kappa)$.

II-2-B. Scattering Formula for Cylindrical Particles in a Paracrystalline Hexagonal Lattice. We assume here that the thermal vibration of the cylinder is frozen at the lattice point for simplicity,

$$D^2(\mathbf{q}) = 1 \tag{13}$$

The cylinders are hexagonally packed, so that the spatial dimensionality d in eqs 5 and 10 is 2.

For the sake of convenience we consider here another Cartesian coordinate $Ox_2y_2z_2$ fixed to the laboratory in which we take the Oz_2 axis parallel to $\mathbf{q}$ and the Ox_2 and Oy_2 axes orthogonal to $\mathbf{q}$. The coordinate $Oxyz$ fixed to the grain is related to the coordinate $Ox_2y_2z_2$ by Eulerian angles (β,η,ϕ) as shown in Figure 3.

Then $(\mathbf{q}\cdot\mathbf{a}_1)$ and $(\mathbf{q}\cdot\mathbf{a}_2)$ in eqs 6–8 are given by

$$\mathbf{q}\cdot\mathbf{a}_1 = \frac{1}{2}q\hat{\mathbf{z}}_2\cdot(\mathbf{b}_1-\mathbf{b}_2) = \frac{1}{2}q[b_1(\hat{\mathbf{z}}_2\cdot\hat{\mathbf{x}}) - b_2(\hat{\mathbf{z}}_2\cdot\hat{\mathbf{y}})] \tag{14}$$

$$\mathbf{q}\cdot\mathbf{a}_2 = q\hat{\mathbf{z}}_2\cdot\mathbf{b}_2 = qb_2(\hat{\mathbf{z}}_2\cdot\hat{\mathbf{y}}) \tag{15}$$

In eqs 14 and 15, $\hat{\mathbf{x}}_2$, $\hat{\mathbf{y}}_2$, and $\hat{\mathbf{z}}_2$ are the unit vectors along Ox_2, Oy_2, and Oz_2, respectively. $\hat{\mathbf{x}}$ and $\hat{\mathbf{y}}$ are the unit vectors along Ox and Oy, respectively, and eqs 1b and 1c were used. Noting that

$$b_1 = \sqrt{3}a, \qquad b_2 = a \tag{16}$$

from eqs 1 and 2 (Figure 1b) and also that

$$\hat{\mathbf{z}}_2\cdot\hat{\mathbf{x}} = -\sin\beta\cos\phi, \qquad \hat{\mathbf{z}}_2\cdot\hat{\mathbf{y}} = \sin\beta\sin\phi \tag{17}$$

we obtain

$$\mathbf{q}\cdot\mathbf{a}_1 = -aq\sin\beta\cos\left(\phi-\frac{\pi}{6}\right) \tag{18}$$

$$\mathbf{q}\cdot\mathbf{a}_2 = aq\sin\beta\sin\phi \tag{19}$$

where the state $\phi = 0°$ was chosen in such a way that $\mathbf{q}\cdot\mathbf{a}_2 = 0$ when $\beta = 90°$ and $\phi = 0°$ (Figures 1b and 3).

The structure amplitude for a cylindrical particle $f(\mathbf{q})$ in eq 4 or 10 with a given orientation shown in Figure 2 is given by

$$f(\mathbf{q}) = 2A_eV\Delta\rho\frac{\sin\left(\frac{qL}{2}\cos\beta\right)}{\frac{qL}{2}\cos\beta}\frac{J_1(qR\sin\beta)}{qR\sin\beta}\times \exp\left[-\frac{1}{2}q^2\sigma_s^2\sin^2\beta\right] \tag{20}$$

where $A_e\Delta\rho$ is the difference in the scattering power between the cylinders and their medium, V is the volume of the cylinders, and σ_s is a parameter characterizing the interface thickness of the cylinders along their radii (see Appendix). We assume that the distribution of the cylinder radius R is given by a Gaussian distribution,

$$P(R) \sim \exp\left[-\frac{(R-\bar{R})^2}{2\sigma_R^2}\right] \tag{21}$$

where $\bar{R}$ and σ_R are the mean radius and a standard deviation of R from $\bar{R}$, respectively. Then $\langle f^n\rangle$ in eq 4 or 10 is given by

$$\langle f^n\rangle = \frac{\int_0^\infty P(R)\,f^n(\mathbf{q};\mathbf{R})\,dR}{\int_0^\infty P(R)\,dR} \tag{22}$$

where $f(\mathbf{q};R)$ denotes the structure amplitude from a single cylinder having a given radius R.

The observed scattered intensity $I(\mathbf{q})$ is obtained by averaging $I(\mathbf{q};\mathbf{n})$ over all possible orientations of the grains,

$$I(q) = \int_0^{2\pi}d\kappa\int_0^{2\pi}d\Omega\int_0^{\pi}d\alpha\; w(\alpha,\Omega,\kappa)\,I(\mathbf{q};\mathbf{n})\sin\alpha \tag{23}$$

or

$$I(q) = \int_0^{2\pi}d\phi\int_0^{2\pi}d\eta\int_0^{\pi}d\beta\; w(\beta,\eta,\phi)\,I(\mathbf{q};\mathbf{n})\sin\beta \tag{24}$$

where $w(\alpha,\Omega,\kappa)$ or $w(\beta,\eta,\phi)$ is a normalized orientation distribution satisfying

$$\int_0^{2\pi} d\kappa \int_0^{2\pi} d\Omega \int_0^{\pi} d\alpha\, w(\alpha,\Omega,\kappa) \sin\alpha = \int_0^{2\pi} d\phi \int_0^{2\pi} d\eta \int_0^{\pi} d\beta\, w(\beta,\eta,\phi) \sin\beta = 1 \quad (25)$$

For a uniform orientation distribution, we have

$$w = 1/(8\pi^2) \quad (26)$$

Thus the equations describing SAS for an assembly of cylinders packed in a hexagonal paracrystal lattice are given by eqs 5–11, 13, 18–22, and 24.

III. Scattering Formula for a Special Case

Let us consider block copolymer films having cylindrical microdomains. The film normal is parallel to Oz_1; i.e., the film surfaces are parallel to Ox_1y_1 in Figure 2. The cylindrical axis **n** in the solvent-cast films tends to be aligned parallel to the film surface such that $\alpha = 90°$ and Ω is random. Let us now consider this special case and the scattering normal to the film surface, i.e., the scattering at the azimuthal angle μ equal to 0°. Under this condition, $\beta = 90°$ and η is random in Figure 3, so that from eqs 2, 3, 5, 6b, 8, 18, and 19

$$Z(q) = Z_1(q)\, Z_2(q) \quad (27)$$

$$Z_1(q) = (1 - \exp[-(\Delta^2 a)q^2 P]) \Big/ \left(1 - 2\exp\left[-\frac{1}{2}(\Delta^2 a)q^2 P\right] \cos\left[aq\cos\left(\phi - \frac{\pi}{6}\right)\right] + \exp[-(\Delta^2 a)q^2 P]\right) \quad (28a)$$

$$Z_2(q) = \frac{1 - \exp[-(\Delta^2 a)q^2 P]}{1 - 2\exp\left[-\frac{1}{2}(\Delta^2 a)q^2 P\right] \cos(aq\sin\phi) + \exp[-(\Delta^2 a)q^2 P]} \quad (28b)$$

where

$$P = \cos^2\left(\phi - \frac{\pi}{6}\right) + \sin^2\phi \quad (28c)$$

$f(\mathbf{q})$ in eq 20 is given by

$$f(q) = 2A_e \Delta\rho V \frac{J_1(qR)}{qR} \exp\left(-\frac{q^2\sigma_s^2}{2}\right) \quad (29)$$

for this special case, since $\beta = 90°$. The meridional scattered intensity $I_\perp(q;\phi)$ in a direction normal to **n** is given by

$$I_\perp(q;\phi) = N[\langle|f^2|\rangle - |\langle f\rangle|^2] + |\langle f\rangle|^2 N_1 N_2 (Z_1 + I_{c1}/N_1)(Z_2 + I_{c2}/N_2) \quad (30a)$$

where I_{c1} and I_{c2} are given by eq 11b. Thus an average meridional scattered intensity $I_\perp(q)$ is obtained by averaging $I_\perp(q;\phi)$ with respect to ϕ,

$$I_\perp(q) = \frac{1}{2\pi}\int_0^{2\pi} I_\perp(q;\phi)\, d\phi \quad (30b)$$

IV. Lorentz Correction: Generalized Scattering Formula for Systems Having an Orientation Distribution

In the case when $L \gg R \gg \lambda$, the scattered intensity from a single cylinder $I_p(\mathbf{q})$ has a nonzero value at q_z satisfying $q_z < 1/L$ and thus at $q_z \cong 0$, where q_z is the component of the scattering vector **q** parallel to the cylindrical axis. Thus from eq 20 and Figure 3,

$$I_p(\mathbf{q}) \sim |f(\mathbf{q})|^2 = 4I_e V^2 \Delta\rho^2 \frac{\sin^2\left(\frac{q_z L}{2}\right)}{\left(\frac{q_z L}{2}\right)^2}\left[\frac{J_1(q_r R)}{q_r R}\right]^2 \times \exp(-\sigma_s^2 q_r^2) \cong 4I_e V^2 \Delta\rho^2 \delta(q_z)\left[\frac{J_1(q_r R)}{q_r R}\right]^2 \exp(-\sigma_s^2 q_r^2) \quad (31)$$

where δ is the delta function,

$$\mathbf{q} = q_x\hat{\mathbf{x}} + q_y\hat{\mathbf{y}} + q_z\hat{\mathbf{z}} \quad (32)$$

and

$$q_r \equiv (q_x^2 + q_y^2)^{1/2} \quad (33)$$

In eqs 32, $\hat{\mathbf{x}}$, $\hat{\mathbf{y}}$, and $\hat{\mathbf{z}}$ are the unit vectors along the Ox, Oy, and Oz axes, respectively. Thus $I_p(\mathbf{q}) = I_p(q_r,q_z)$ is the δ function along q_z at a given q_r. An appreciable intensity exists in reciprocal space only in the plane passing through its origin and normal to the cylinder axis.

Similarly, the scattered intensity $I(\mathbf{q};\mathbf{n})$ from the grains (Figure 4a) has nonzero intensity only in the plane π which passes through $q_z = 0$ in reciprocal space and is perpendicular to the cylinder axis **n**. The scattering has a cylindrically symmetric intensity distribution with respect to **n** if ϕ is random as schematically shown in Figure 4b; i.e.,

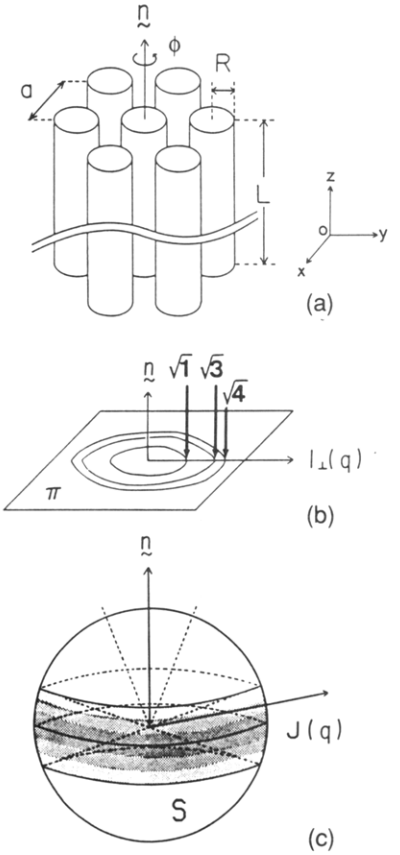

Figure 4. (a) A paracrystal having $L \gg R$. (b) The scattered intensity distribution for the paracrystal shown in part a is localized in the plane π normal to **n** and through the origin in reciprocal space. The rotational angle ϕ is assumed to be random. (c) The scattered intensity distribution for the paracrystal having an orientation distribution in three-dimensional space.

$$I(\mathbf{q};\mathbf{n}) \cong \delta(q_z)\, I_\perp(q) \tag{34}$$

where $I_\perp$ is the intensity at q in a given direction normal to $\mathbf{n}$ (see Figure 4b). Here, $q \equiv q_r$; i.e., we suppressed the subscript r for the sake of convenience. The total scattered intensity $Q(q)$ from the grain at a given q normal to $\mathbf{n}$ is then given by

$$Q(q) = 2\pi q I_\perp(q) \tag{35}$$

In the case when the paracrystal grain has an orientation distribution with respect to any given laboratory axis, the scattered intensity localized in the plane π is distributed on a surface of sphere S in reciprocal space as schematically shown in Figure 4c. Thus the total scattered intensity $Q(q)$ is given by

$$Q(q) \sim J(q)q^2 \tag{36}$$

where $J(q)$ is the intensity distribution measured along any given direction in reciprocal space. The total intensity given by eq 35 should be physically identical to that given by eq 36. Hence we obtain

$$J(q) \sim q^{-1} I_\perp(q) \tag{37}$$

The prefactor q^{-1} is the Lorentz factor, some features of which were discussed extensively in a previous paper.[5] Equation 37 can be applied for any system having a given orientation except for a perfectly oriented system which exists mathematically as a singular point and for which $J(q)$ normal to $\mathbf{n}$ is given by

$$J(q) \sim I_\perp(q) \tag{38}$$

It is obvious that the intensity $I_\perp(q)$ can be calculated from $I_\perp(q;\phi)$ given by eq 30.

Now let us try to investigate eq 36 in detail and in a different way for the systems whose orientation distribution $w(\alpha,\Omega,\kappa)$ is specified in terms of the coordinate $Ox_1y_1z_1$ shown in Figure 2. The scattered intensity distribution with q at a given azimuthal angle μ, $I(q,\mu)$, depends on a number density of the paracrystals whose axes $\mathbf{n}$ orient normal to the vector $\mathbf{q}$ specified by 2θ and μ. Since the structure dealt with here is assumed to be independent of its orientation, the relative intensity distribution with q is independent of μ, and hence $I(q,\mu)$ is written by

$$I(q,\mu) = J(q)\, F(\mu) \tag{39}$$

$F(\mu)$ depends on the number density of the paracrystals contributing to the scattering at this μ. If we consider a case in which the paracrystals are uniaxially oriented with respect to the Oz_1 axis, for the sake of simplicity in our argument, the total intensity $Q(q)$ is given by

$$\begin{aligned} Q(q) &= \int_0^\pi I(q,\mu)(2\pi q^2) \sin\mu \, d\mu \\ &= 2\pi q^2 J(q) \int_0^\pi F(\mu) \sin\mu \, d\mu \end{aligned} \tag{40}$$

Thus we can obtain eq 36. Similarly, we can prove eq 36 for a biaxial orientation of the paracrystals.

V. Numerical Analyses

Numerical analyses for the scattering from the cylinders with the hexagonal paracrystal lattice were performed for the following cases: (i) $a_1 = a_2 = a$ and $\Delta^2 a_{ij} = \Delta^2 a$ or $g_{ij} = g = (\Delta^2 a/a^2)^{1/2}$ $(i,j = 1,2)$, i.e., the case in which eqs 2 and 3 are satisfied; (ii) the rotation of the crystals around the cylinder axis is uniform, i.e., the case in which the angle ϕ in Figure 3 or κ in Figure 2 is random; (iii) the size of the paracrystal $N = N_1N_2$ is infinite so that the zeroth-order scattering I_{ck} becomes insignificant, and (iv) $D^2(\mathbf{q}) = 1$. In this case eq 10 is simplified as

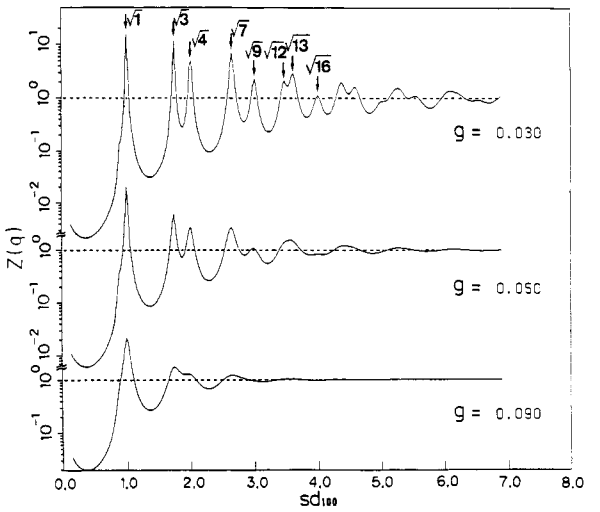

Figure 5. Effects of the paracrystal distortion factor g on the lattice factor $Z(q)$. The higher order maxima are seen at the scattering vector satisfying $sd_{hk0} = 1$, where d_{hk0} is given by eq 45. The scattering vector s is related to q by $q = 2\pi s$.

$$I(\mathbf{q};\mathbf{n})/N = \langle|f^2|\rangle - |\langle f\rangle|^2 + |\langle f\rangle|^2 Z_1 Z_2 \tag{41}$$

The q dependence of the scattered intensity in a given direction in the reciprocal space $J(q)$ was calculated either by using eqs 24 and 41 ("full" intensity distribution) or by using eq 37 ("Lorentz-corrected" intensity distribution), where $I_\perp$ in eq 37 is obtained from eq 30b and $I_\perp(q;\phi)$ in eq 30b is simplified similarly to eq 41

$$I_\perp(q;\phi)/N = \langle|f^2|\rangle - |\langle f\rangle|^2 + |\langle f\rangle|^2 Z_1 Z_2 \tag{42}$$

V-1. Paracrystal Lattice Factor Z. From eqs 27 and 28, the paracrystal lattice factor Z was numerically estimated by averaging it with ϕ. For the numerical analyses, it is important to note that the lattice factor Z is a sharp function of ϕ at about the values satisfying

$$[1 - \cos(aq \sin\phi)]\{1 - \cos[aq \cos(\phi - \pi/6)]\} \cong 0 \tag{43}$$

Figure 5 shows the results for $Z(q)$ at paracrystal distortion factors $g = 0.03$, 0.05, and 0.09 plotted as a function of reduced scattering vector sd_{100}, where $s = q/2\pi = 2(\sin\theta)/\lambda$ and d_{100} is the lattice spacing of the (100) plane. The spacing d_{100} is related to the cell edge a

$$d_{100} = (\sqrt{3}/2)a \tag{44a}$$

so that

$$sd_{100} = (\sqrt{3}/4\pi)aq \tag{44b}$$

As seen in Figure 5, Z has a series of sharp higher order maxima at the reduced scattering vectors 1, $\sqrt{3}$, $\sqrt{4}$, $\sqrt{7}$, $\sqrt{9}$, $\sqrt{12}$, $\sqrt{13}$, $\sqrt{16}$, ... relative to that of the first-order maximum. These positions of the higher order maxima are given by

$$sd_{hk0} = \sqrt{h^2 + hk + k^2} \quad (h,k, \text{integers}) \tag{45}$$

and correspond respectively to d_{100}, d_{110}, d_{200}, d_{210}, d_{300},

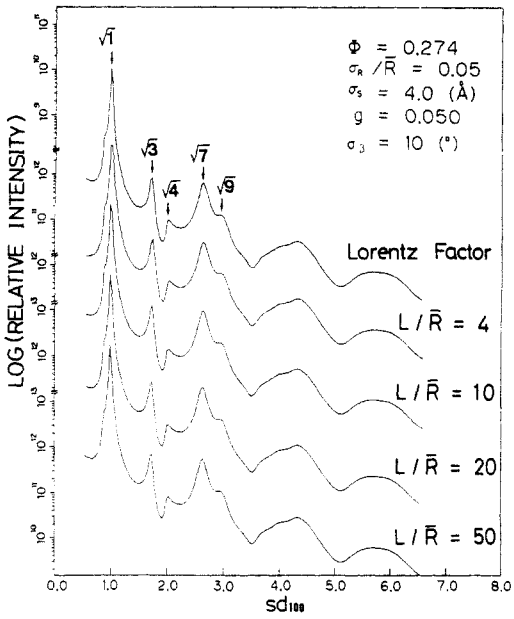

Figure 6. Comparison between the "Lorentz-corrected" intensity profile (the profile designated "Lorentz Factor") and the "full" intensity profiles for the paracrystals having various aspect ratios $L/\bar{R}$ for a given set of the parameters ($\Phi = 0.274$, $\sigma_R/\bar{R} = 0.05$, $\sigma_s = 4.0$ Å, $g = 0.05$, and $\sigma_\beta = 10°$).

d_{220}, d_{310}, d_{400}, ..., where d_{hk0} is the lattice spacing of the $(hk0)$ planes. It is obvious that the higher order peaks damp away to the asymptotic value of unity, more rapidly with increasing paracrystal distortion factor g, which provides an experimental basis to determine the value g.

V-2. Lorentz Correction. Figure 6 compares the "Lorentz-corrected" scattered intensity profile (the top profile designated by "Lorentz Factor") with the "full" intensity profiles calculated for various aspect ratios L/R and for a given set of the parameters characterizing the paracrystals, $\Phi = 0.274$, $\sigma_R/\bar{R} = 0.05$, $\sigma_s = 4.0$ Å, $g = 0.05$, and $\sigma_\beta = 10°$, where Φ is the volume fraction of cylinders,

$$\Phi = (2\pi/\sqrt{3})(\bar{R}/a)^2 \tag{46}$$

and σ_β is the parameter characterizing the breadth of the orientation distribution of the cylinders with respect to β. We assume here the following orientation distribution function:

$$W(\beta) = (\text{const}) \exp(-|\beta - 90°|^2/2\sigma_\beta^2) \tag{47}$$

It is clearly shown that the Lorentz-corrected profile becomes essentially identical to the full intensity profiles for cylinders having an aspect ratio $L/R \geq 4$, although the Lorentz-corrected profile is theoretically expected to be rigorous for the limit of $L/R \to \infty$. For the cylindrical microdomains found in the block copolymers, L/R is very likely to be greater than 4. Therefore the Lorentz-corrected profiles can be used in practice as theoretical profiles and can be compared with experimental profiles to obtain the paracrystal parameters. The full intensity profiles for the assembly of cylinders having an aspect ratio $L/2\bar{R} < 2$ were not shown here, though a comparison of the full intensity profile with the Lorentz-corrected intensity profiles for such cylinders may be interesting. This is simply because for such an assembly of short cylinders it is very likely that we must take into account the axial correlation of cylinders, which we ignore in our model (section II-1). Thus the assembly brings us a new problem which is beyond scope of the present work. We hereafter show only the Lorentz-corrected scattering profiles.

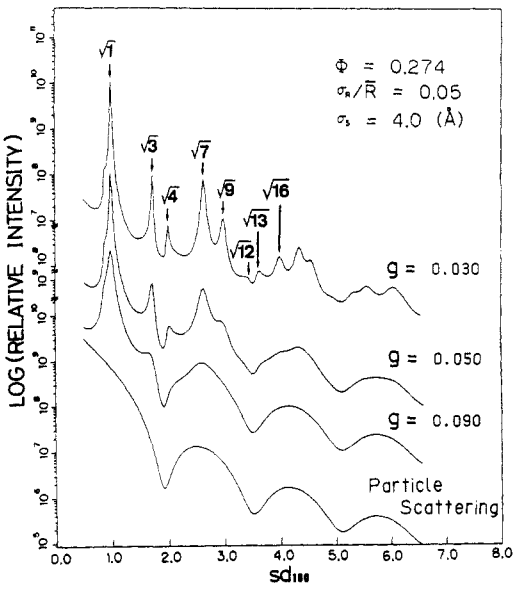

Figure 7. Effect of the paracrystal distortion factor g on the scattered intensity profiles. The scattering from a single cylinder (designated "Particle Scattering") having $\bar{R}$ specified by Φ is shown as a reference.

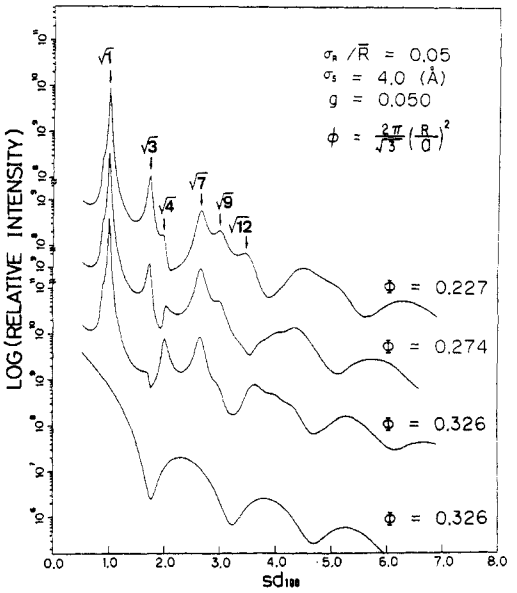

Figure 8. Effect of the volume fraction of the cylinders on the scattering profiles from the paracrystal and the scattering from a single cylinder (the profile at the bottom) having $\bar{R}$ specified by Φ.

V-3. Paracrystalline Distortion Factor. Since the paracrystalline distortion factor g affects the theoretical intensity profile only through the paracrystal lattice factor Z, its effect on Z was discussed in section V-1. However, the effect of g on the scattering profiles is not intuitively clear, because the profiles are also affected by the form factor of the particles on the lattice. Thus we show the effect of the paracrystal distortion factor g on the "Lorentz-corrected" scattering profiles in Figure 7, together with the scattering profile from a single cylinder (designated as "Particle Scattering"), for a given set of the parameters $\Phi = 0.274$, $\sigma_R/\bar{R} = 0.05$, and $\sigma_s = 4.0$ Å. As g increases, the higher order peaks tend to damp out, and the profile is reduced to the particle scattering profile.

V-4. Estimation of Volume Fraction of Cylinders. Figure 8 shows the effects of the volume fraction of cylinders on the scattering profiles for a fixed set of the paracrystalline parameters $g = 0.05$, $\sigma_R/\bar{R} = 0.05$, and $\sigma_s = 4.0$ Å, together with the particle scattering factor for a

Table 1. Molecular Characteristics of PS–PEP Diblock Copolymers

sample code	M_n[a]	M_w/M_n[b]	W_{PS}[c] (%)	f_{PS}[d]	morphology
K2	3.2×10^4	1.5	38.7	0.339	lamella
K3	3.4×10^4	1.3	12.4	0.103	sphere

[a] Number-average molecular weight determined from a membrane osmometer. [b] Heterogeneity index determined from size exclusion chromatography. [c] Weight fraction of polystyrene block in the copolymer determined from ^{13}C NMR. [d] Volume fraction of polystyrene block in the copolymer calculated with W_{PS} and the densities of PS (1.06 g/cm^3) and PEP (0.86 g/cm^3).

cylinder having the radius $\bar{R}$ as determined from $\Phi = 0.326$ as a reference. It should be noted that the relative intensities of the higher order maxima, in this particular case those at $\sqrt{3}$ and $\sqrt{4}$, are very sensitive to the change of Φ. This factor provides a basis for the experimental determination of the volume fraction of cylinders in the lattice. The positions of the broad particle scattering maxima are different from those in Figure 7, which reflects the difference in the value $\bar{R}$. The peak positions of the broad particle scattering maxima provide a method to evaluate $\bar{R}$, and those of the sharp maxima from the lattice spacings d_{hk0} provide a method to evaluate a. The values $\bar{R}$ and a also determine the value Φ. This value should be consistent with the value determined from the relative peak heights.

VI. Comparison with Experimental Scattering Profile

In this section we apply the scattering theory described above to SAXS from a binary mixture of PS–PEP diblock copolymers and try to characterize its unique microdomain structure.

VI-1. Block Copolymer Samples. The molecular characteristics of the PS–PEP diblock copolymers used in this work are summarized in Table 1. The copolymers were kindly supplied by the Research Laboratory, Kurare Co. Ltd., Japan. The samples coded K2 and K3, which were prepared especially for our research, were synthesized by living anionic polymerization to create a polystyrene-*block*-polyisoprene precursor, followed by selective hydrogenation of the polyisoprene block. The size exclusion chromatograms of the PS–PEP copolymers showed a broad single peak as characterized by the heterogeneity index in Table 1. Film specimens of the 50/50 wt/wt blend of K2/K3 as well as those for the neat copolymers K2 and K3 were prepared by the solution-cast method in which a 5 wt % solution of each copolymer system was cast into films of ~0.5-mm thickness by slowly evaporating the solvent (toluene) at 30 °C over 10 days. The as-cast films were further annealed at 150 °C for 30 min.

The microdomain structures formed in the films were examined by transmission electron microscopy (TEM) and SAXS. For TEM observation, the films were first stained by RuO_4 vapor and subsequently cut into ultrathin sections of ~500 Å at −85 °C by using an ultramicrotome (LKB 4800A Ultratome) with a diamond knife. The sections on the electron microscope grids were further stained by RuO_4 vapor for a few hours. Electron microscopy observation was done with a Hitachi H7000 transmission electron microscope operated at 100 kV. The SAXS profiles were obtained by a method described elsewhere[9] and corrected for air scattering, thermal diffuse scattering, and slit-width and slit-height smearing effects.

Figure 9 shows a typical TEM micrograph for copolymer K2 in which the bright and dark phases correspond to lamellae composed of poly(ethylenepropylene) (PEP) block chains unstained by RuO_4 and lamellae composed of polystyrene (PS) block chains stained by RuO_4, respectively. The micrographs represent a regular alternating lamellar microdomain structure composed of PEP lamellae and PS lamellae. The lamellar assembly has a grain structure detailed elsewhere,[10] and each grain has a different orientation with respect to its lamellar normal. Thus when the incident X-ray beam is irradiated normal to the film surface, the SAXS patterns taken normal to the incident beam show a series of diffraction rings with a circularly symmetric intensity distribution with respect to the incident beam axis.

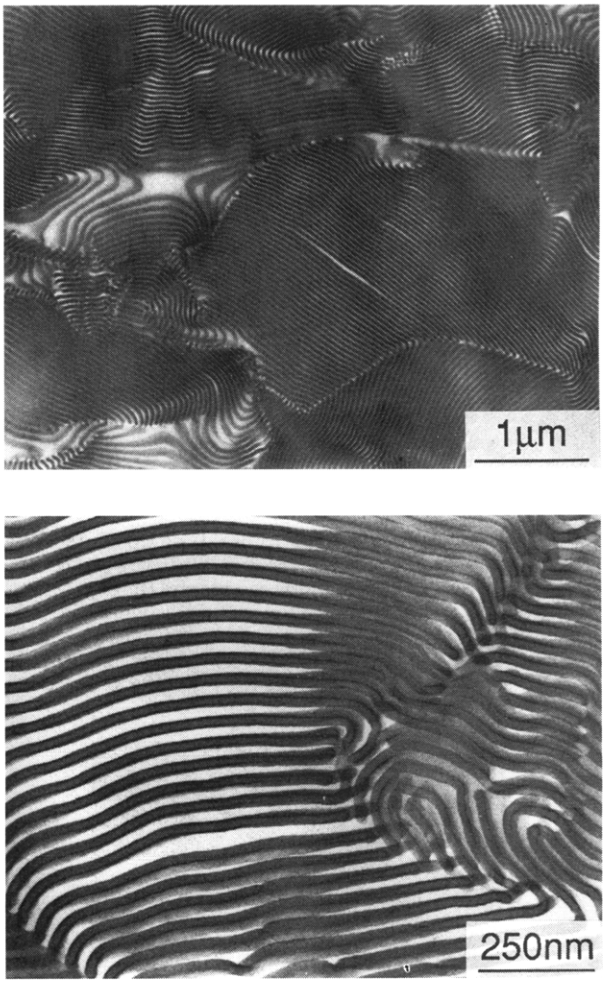

Figure 9. Transmission electron micrograph for the PS–PEP specimen K2, showing alternating dark and bright lamellae composed of the PS and PEP block chains, respectively.

Figure 10 shows the SAXS intensity profile for K2, in which the profile shown by the dots was experimentally obtained and that shown by the solid line is the theoretical profile for the alternating lamellar assembly with paracrystal distortions[2b] which is best fitted to the experimental profile according to the method described in section VI-2. The best-fitting procedure yields the parameters characterizing the lamellar structure: the lamellar identity period $d = 349.0 \pm 1.0$ Å, the paracrystal distortion factor of the lamellar assembly $g = (3.20 \pm 0.15) \times 10^{-2}$, the volume fraction of PS lamellae $\Phi_{PS} = (3.15 \pm 0.06) \times 10^{-1}$, the standard deviation in thickness distribution of PS lamellae $\sigma_{PS} = 5.2 \pm 1.0$ Å, and the characteristic interface thickness between PS and PEP lamellae $t \equiv (2\pi)^{1/2}\sigma_s = 20 \pm 15$ Å. The large error involved in the estimation of t will be discussed in section VI-3.

Figure 11 presents the TEM micrograph obtained for K3. The micrograph shows spherical microdomains of

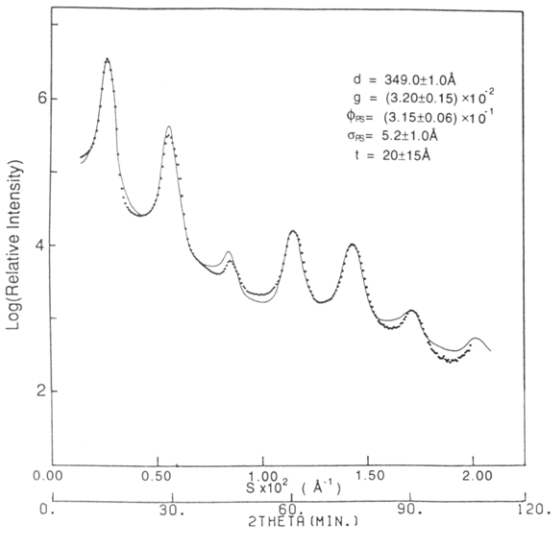

Figure 10. Experimental (shown by dots) and calculated SAXS profiles (shown by a solid line) for the PS–PEP specimen K2. The best fit between the calculated profile and the experimental profile over the entire q range covered in this work yielded an optimal set of structure parameters: $d = 349.0 \pm 1.0$ Å, $g = (3.20 \pm 0.15) \times 10^{-2}$, $\Phi_{PS} = (3.15 \pm 0.06) \times 10^{-1}$, $\sigma_{PS} = 5.2 \pm 1.0$ Å or $t = 20 \pm 15$ Å. t can be estimated with a better accuracy (see the comment in section VI-3).

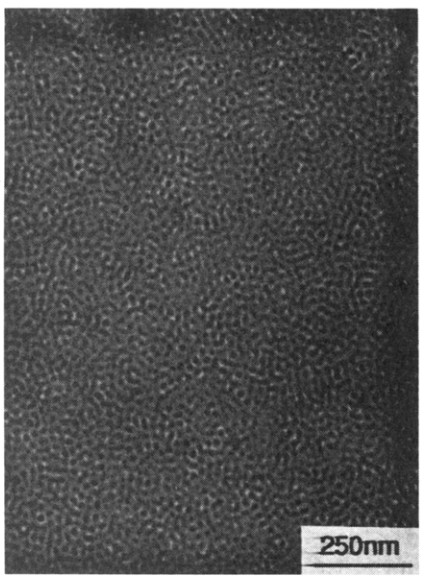

Figure 11. Transmission electron micrograph for the PS–PEP specimen K3, showing the spheres composed of the PS block chains dispersed in the matrix composed of the PEP block chains. The spheres appear to be interconnected, due to the facts that they overlap along the thickness direction of the ultrathin specimens and that they are packed in a cubic lattice with a large paracrystal distortion factor g.

PS block chains dispersed in the matrix of PEP block chains. The spheres appear to be connected, which is an artifact due to overlap along the thickness direction of the ultrathin specimen. The artifact is believed to be the result of (i) the small radius of the spheres and interparticle distance relative to the thickness of the ultrathin sections prepared for the TEM observation and (ii) the large paracrystal distortion factor g.

Figure 12 shows the SAXS profile for K3. The experimental profile is shown by dots. The solid line shows the theoretical profile for isolated spheres[7] with the size distribution given by a Gaussian distribution with mean radius $\bar{R} = 70.6 \pm 0.25$ Å, standard deviation $\sigma_R = 15.1 \pm 0.35$ Å, and characteristic interface thickness $t = 13.3 \pm 0.88$ Å. The thin arrows indicate intersphere interference

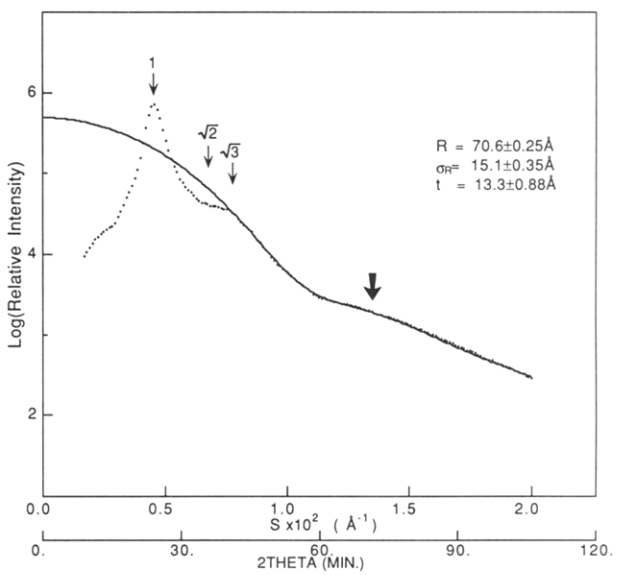

Figure 12. Experimental SAXS profile for the PS–PEP specimen K3 (shown by dots) and the calculated profile (shown by the solid line) for a single sphere best fitted to the experimental profile. The best fit yielded $\bar{R} = 70.6 \pm 0.25$ Å, $\sigma_R = 15.1 \pm 0.35$ Å, and $t = 13.3 \pm 0.88$ Å.

maxima or shoulders expected for a cubic symmetry, located at the scattering vectors 1, $\sqrt{2}$, and $\sqrt{3}$ relative to that of the first-order maximum, while the broad maximum marked by the thick arrow indicates that from the form factor of the isolated spheres.

VI-2. Method of Parameter Estimation. We define $\mathbf{P} \equiv \{p_1, p_2, ..., p_m\}$ as a parameter set that we obtain by the best fitting of the calculated scattering curve $I_{theo}(q_i;\mathbf{P})$ $(i = 1, ..., n)$ and the experimental scattering curve $I_{exp}(q_i)$ $(i = 1, ..., n)$, where q_i is the scattering vector at which the scattering intensity is calculated for a given set of the parameters $[I_{theo}(q_i;\mathbf{P})]$ or measured $[I_{exp}(q_i)]$. We define $\sigma(q_i)$ $(i = 1, ..., n)$ as an error between $I_{theo}(q_i;\mathbf{P})$ and $I_{exp}(q_i)$ at q_i. The statistical errors in the photon counting of the scattered X-rays are also included in $\sigma(q_i)$. In our experiments, the scattered X-ray photons typically vary from 5×10^5 to 150 counts with q, corresponding to $\sigma_{N_P}/N_P = 0.001$–0.08, where σ_{N_P} and N_P are the standard deviation in the number of photons counted and the mean value of the photons counted, respectively. $\mathbf{P}$ consists of structural parameters such as a, g, $\bar{R}$, σ_R, and σ_s. The probability density $L(\mathbf{P})$ that $\mathbf{P}$ is the parameter set to be expected is given by

$$L(\mathbf{P}) = (2\pi)^{-n/2}[\prod_{i=1}^{n}\sigma(q_i)]^{-1}\exp\left[-\frac{1}{2}S(\mathbf{P})\right] \quad (48)$$

$$S(\mathbf{P}) = \sum_{i=1}^{n}\{I_{exp}(q_i) - I_{theo}(q_i;\mathbf{P})\}^2/\sigma(q_i)^2 \quad (49)$$

The minimization of $S(\mathbf{P})$ gives rise to the maximization of $L(\mathbf{P})$. This provides a basis for an optimization program such as that given below.

We first assign an initial trial set of parameters $\mathbf{P} = \{p_1^{(0)}, p_2^{(0)}, ..., p_m^{(0)}\}$. We vary p_1 around $p_1^{(0)}$ and calculate $S(\mathbf{P})$. We determine $p_1^{(1)}$ which minimizes $S(\mathbf{P})$. Similarly, we determine other parameters $p_2^{(1)}$, ..., and $p_m^{(1)}$. We calculate $S(\mathbf{P})$ for the new set of parameters $\mathbf{P} = \{p_1^{(1)}, p_2^{(1)}, ..., p_m^{(1)}\}$. We define the new set of the parameters $\mathbf{P} = \{p_1^{(1)}, p_2^{(1)}, ..., p_m^{(1)}\}$ as the second trial set of parameters $\mathbf{P}$ and repeat the above procedure to determine $\mathbf{P} = \{p_1^{(2)}, p_2^{(2)}, ..., p_m^{(2)}\}$. We repeat this process until $S(\mathbf{P})$ converges

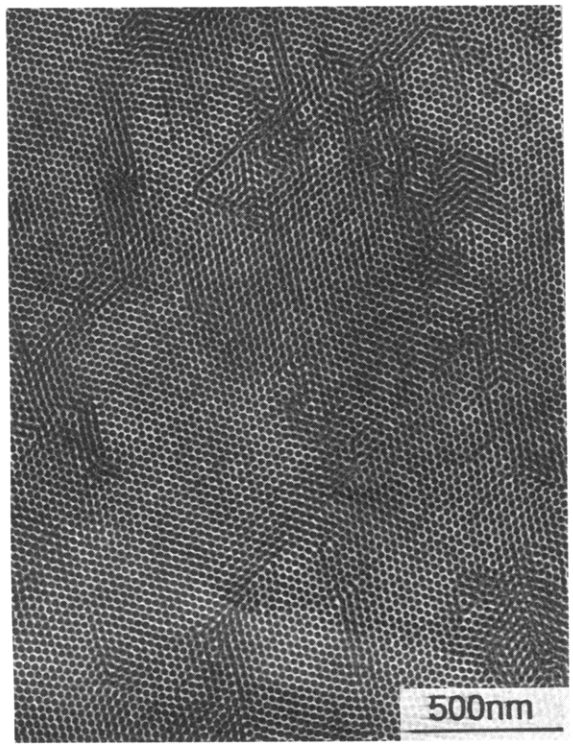

Figure 13. Transmission electron micrograph of the PS–PEP/PS–PEP K2/K3 50/50 wt/wt mixture, showing hexagonally packed cylindrical microdomains composed of the PS block chains dispersed in the matrix composed of the PEP block chains. The two copolymers K2 and K3 are mixed in the microdomains with their junctions at the interfaces and the PS and PEP block chains segregated in the respective domains.

to the preassigned value. The set **P** which gives the convergence is regarded to be our best optimum solution $\mathbf{P}^* = \{p_1^{(k)}, p_2^{(k)}, ..., p_m^{(k)}\}$.

We estimate an error $\sigma_{p_i}^{(k)}$ for the parameter $p_i^{(k)}$ thus obtained as follows. We vary p_i around $p_i^{(k)}$ and calculate $L(\mathbf{P}=\{p_1^{(k)},p_2^{(k)},...,p_i,...,p_m^{(k)}\})$, $L(\mathbf{P}^*)$, and

$$F(p_i) \equiv L(\mathbf{P}=\{p_1^{(k)},...,p_i,...,p_m^{(k)}\})/L(\mathbf{P}^*) \qquad (50)$$

$F(p_i)$ is approximated by a Gaussian function centered at $p_i = p_i^{(k)}$ and then the standard deviation σ_{p_k} is obtained. Similarly, we determine a set of the standard deviations $\mathbf{\Sigma} \equiv (\sigma_{p_1}, \sigma_{p_2}, ..., \sigma_{p_m})$ for the optimal parameter set $\mathbf{P}^* = \{p_1^{(k)}, p_2^{(k)}, ..., p_m^{(k)}\}$ that results from the specific numerical method applied for the data analysis.

VI-3. Comparison between Experimental and Theoretical Profiles for a Cylindrical System. The K2/K3 binary blend with 50/50 wt/wt composition was investigated by TEM. Figure 13 shows a typical TEM micrograph, indicating the hexagonally packed cylinders of the PS block chains dispersed in the matrix of the PEP block chains. This image corresponds to that obtained in the section on which the cylindrical axes orient nearly normal to it. The assembly of cylinders has a grain structure similar to that in the lamellar assembly shown in Figure 9, so that the cylindrical axis **n** has an orientation variation from one grain to another. The micrograph clearly shows that the two copolymers K2 and K3 are uniformly mixed in the microdomain space with their PS and PEP block chains in the PS and PEP microdomains, respectively, and their chemical junctions at the interface between the two domains.

Figure 14 shows the experimental SAXS profile with dots and the best-fitted calculated profile with a solid line. A good agreement between the experimental and calculated profiles was obtained, yielding the optimal set of characteristic parameters $\bar{R} = 78.2 \pm 1.5$ Å, $\sigma_R = 10.8 \pm 2.0$ Å, $\sigma_s = 6.7 \pm 5.1$ Å (or $t = 16.8 \pm 12.8$ Å), $a = 360.5 \pm 1.0$ Å, and $g = (4.70 \pm 0.22) \times 10^{-2}$. It should be noted that each parameter affects the net profile in a different way. This fact and the fact that there are sufficiently large numbers of scattering peaks facilitate an unequivocal determination of these parameters. Here it is worth noting a possible origin of the large error estimation of σ_s or t induced by our method used in this work (section VI-2). As is obvious from the scattering theory described in section III or IV, the parameter associated with the interface thickness σ_s or t affects $I_{exp}(q_i)$ only at large q_i or $s_i \equiv s$, typically $s \gtrsim 1 \times 10^{-2}$ Å^{-1} in Figure 14. However, the error estimation program used in this work involved the calculation of $F(p_i)$ ($p_i = \sigma_s$ or t in this case) in eq 50 for all q_i covered in this experiment, including not only the large q_i values relevant to the estimation of σ_s or t but also the small q_i values. Since a small change of σ_s or t does not cause a significant change of $S(\mathbf{P})$ at the small q_i's and the contribution of the data $S(\mathbf{P})$ at these small q_i's to $F(p_i)$ is significant, the small change of σ_s or t does not cause a significant change in $F(p_i)$. This is a primary reason for the large error estimation. Thus a better estimation of σ_s or t can be accomplished by estimating $F(p_i)$ for the data in the relevant q range. In fact, the error estimation for t in Figure 12 is much smaller than that in Figure 10 or 14, simply because $F(p_i)$ was estimated for the data in the relevant q or s range, i.e., $s \gtrsim 0.75 \times 10^{-2}$.

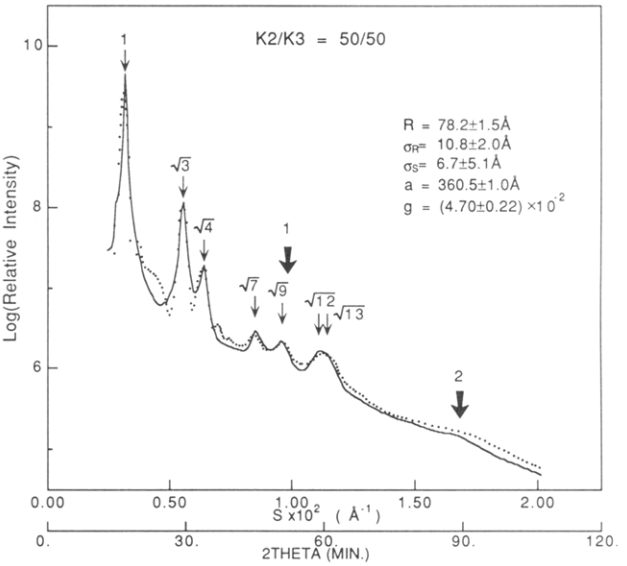

Figure 14. Comparison between the experimental SAXS profile (dots) and the best-fitted calculated scattering profile (solid line) for the PS–PEP/PS–PEP K2/K3 50/50 wt/wt mixture. The best fit gave a set of the parameters for the cylindrical system: $\bar{R} = 78.2 \pm 1.5$ Å, $\sigma_R = 10.8 \pm 2.0$ Å, $\sigma_s = 6.7 \pm 5.1$ Å, $a = 360.5 \pm 1.0$ Å, and $g = (4.70 \pm 0.22) \times 10^{-2}$. See the comment in section VI-3 for the large error estimation of σ_s.

It should also be noted that the deviation of the experimental profile from the calculated profile in the angular region between the right-hand side of the first-order peak and the left-hand side of the third-order peak (at $\sqrt{4}$ relative to the position of the first-order peak) is believed to be due to artifacts related to the instability of the desmearing procedure. Thin arrows indicate the scattering maxima arising from the intercylinder interference, while the thick arrows marked by numbers 1 and 2 indicate respectively the first- and second-order maxima from the form factor of the single cylinders.

VII. Conclusions

We have presented the formula for elastic small-angle scattering from hexagonally packed cylindrical particles with paracrystal distortions. The numerical analysis of the scattering curves was performed to investigate the accuracy of the "Lorentz-corrected" scattered intensity profile as well as to investigate the effects of the paracrystal distortion factor g and the volume fraction of cylinders on the scattering profiles. The Lorentz-corrected profile was found to be correct for most of the practical cases in which the aspect ratio of the cylinders $L/R \geq 4$. A good agreement was obtained between a calculated profile and an experimental SAXS profile for a hexagonally packed cylindrical system, providing a unique determination of various parameters such as $\bar{R}$, σ_R, σ_s, a, and g.

Appendix. Scattering from a Cylindrical Particle with a Diffuse Interface

We define $\rho_{obs}(\mathbf{r})$ and $\rho_0(\mathbf{r})$ as the spatial distribution of a scattering contrast with and without a diffuse boundary, respectively. $\rho_{obs}(\mathbf{r})$ is given by a convolution product of $\rho_0(\mathbf{r})$ and a smoothing function $h(\mathbf{r})$ which determines a diffuseness of the boundary for a cylindrical particle,

$$\rho_{obs}(\mathbf{r}) = \rho_0(\mathbf{r}) * h(\mathbf{r}) = \int \rho_0(\mathbf{u})\, h(\mathbf{r}-\mathbf{u})\, d\mathbf{u} \qquad \text{(A1)}$$

The scattering amplitude $f(\mathbf{q})$ from the particle is then given by

$$f(\mathbf{q}) = \mathcal{F}\{\rho_{obs}(\mathbf{r})\} = \mathcal{F}\{\rho_0(\mathbf{r})\}\, \mathcal{F}\{h(\mathbf{r})\} \qquad \text{(A2)}$$

where $\mathcal{F}\{x(r)\}$ designates the Fourier transform of the function $x(\mathbf{r})$. $f_0(\mathbf{q};\mathbf{n}) \equiv \mathcal{F}\{\rho_0(\mathbf{r})\}$ is well known and is given by

$$f_0(\mathbf{q};\mathbf{n}) = 2A_e V \Delta\rho \frac{\sin\left(\frac{qL}{2}\cos\beta\right)}{\frac{qL}{2}\cos\beta} \frac{J_1(qR\sin\beta)}{qR\sin\beta} \qquad \text{(A3)}$$

for the cylinder with a given orientation $\mathbf{n}$ with respect to the coordinate shown in Figure 3.

In the case when the cylinder has different interface thicknesses σ_z and σ_s along the directions parallel and perpendicular to the cylindrical axis, respectively, $h(\mathbf{r})$ is given by

$$h(\mathbf{r}) = h_1(\rho_r)\, h_2(z) \qquad \text{(A4)}$$

with

$$h_1(\rho_r) = (2\pi\sigma_s^2)^{-1} \exp(-\rho_r^2/2\sigma_s^2) \qquad \text{(A5)}$$

$$h_2(z) = (2\pi\sigma_z^2)^{-1/2} \exp(-z^2/2\sigma_z^2) \qquad \text{(A6)}$$

and

$$\int_0^\infty h_1(\rho_r)(2\pi\rho_r)\, d\rho_r = \int_{-\infty}^{\infty} h_2(z)\, dz = 1 \qquad \text{(A7)}$$

Here the interface thickness is assumed to be cylindrically symmetric and ρ_r is the radial coordinate normal to the cylinder. From eqs A4–A7, we obtain

$$H(\mathbf{q}) = \mathcal{F}\{h(\mathbf{r})\} = \exp\left[-\frac{1}{2}(\sigma_z^2 \cos^2\beta + \sigma_s^2 \sin^2\beta)q^2\right] \qquad \text{(A8)}$$

In the case when $\sigma_z = 0$, we obtain eq 20 from eqs A2, A3, and A8.

References and Notes

(1) Guinier, A.; Fournet, G. *Small-Angle Scattering of X-rays*; Wiley: New York, 1955. Brumberger, H., Ed. *Small-Angle X-ray Scattering*; Gordon and Breach: New York, 1967. Glatter, O.; Kratky, O., Eds. *Small Angle X-ray Scattering*; Academic Press: London, 1982. See also: *J. Appl. Crystallogr.* **1991**, *24*, 413–974 (8th International Conference on Small-Angle Scattering, Leuven, Belgium, Aug 6–9, 1990).

(2) (a) Hashimoto, T.; Nagatoshi, K.; Todo, A.; Hasegawa, H.; Kawai, H. *Macromolecules* **1974**, *7*, 364. (b) Shibayama, M.; Hashimoto, T. *Macromolecules* **1986**, *19*, 740.

(3) Matsuoka, H.; Tanaka, H.; Hashimoto, H.; Ise, N. *Phys. Rev.* **1987**, *B36*, 1754. Matsuoka, H.; Tanaka, H.; Iizuka, N.; Hashimoto, T.; Ise, N. *Phys. Rev.* **1990**, *B41*, 3854.

(4) Hosemann, R.; Bagchi, S. N. *Direct Analysis of Diffraction by Matter*; North-Holland: Amsterdam, 1962.

(5) Shibayama, M.; Nomura, S.; Hashimoto, T.; Thomas, E. L. *J. Appl. Phys.* **1989**, *66*, 4188.

(6) Hashimoto, T.; Todo, A.; Itoi, H.; Kawai, H. *Macromolecules* **1977**, *10*, 377. Hashimoto, T.; Shibayama, M.; Kawai, H. *Macromolecules* **1980**, *13*, 1237; **1983**, *16*, 1093. Sakurai, S.; Okamoto, S.; Kawamura, T.; Hashimoto, T. *J. Appl. Crystallogr.* **1991**, *24*, 679. Hasegawa, H.; Tanaka, H.; Hashimoto, T.; Han, C. C. *J. Appl. Crystallogr.* **1991**, *24*, 672.

(7) Todo, A.; Uno, H.; Miyoshi, K.; Hashimoto, T.; Kawai, H. *Polym. Eng. Sci.* **1977**, *17*, 587. Todo, A.; Hashimoto, T.; Kawai, H. *J. Appl. Crystallogr.* **1978**, *11*, 558. Hashimoto, T.; Fujimura, M.; Kawai, H. *Macromolecules* **1980**, *13*, 1660. Fujimura, M.; Hashimoto, H.; Kurahashi, K.; Hashimoto, T.; Kawai, H. *Macromolecules* **1981**, *14*, 1196. Hashimoto, H.; Fujimura, M.; Hashimoto, T.; Kawai, H. *Macromolecules* **1981**, *14*, 844. Shibayama, M.; Hashimoto, T.; Kawai, H. *Macromolecules* **1983**, *16*, 1437.

(8) Hashimoto, T.; Todo, A.; Kawai, H. *Polym. J.* **1978**, *10*, 521.

(9) Hashimoto, T.; Suehiro, S.; Shibayama, M.; Saijo, K.; Kawai, H. *Polym. J.* **1981**, *13*, 501. Suehiro, S.; Saijo, K.; Ohta, Y.; Hashimoto, T.; Kawai, H. *Anal. Chim. Acta* **1986**, *189*, 41. Fujimura, M.; Hashimoto, T.; Kawai, H. *Mem. Fac. Eng., Kyoto Univ.* **1981**, *43*, 224.

(10) Nishikawa, Y.; Kawada, H.; Hasegawa, H.; Hashimoto, T. *Acta Polym.* **1993**, *44*, 192.